DEM investigation of sand response during displacement pile installation

Nuo Duan[a, c], Yi Pik Cheng[c], Mingfei Lu[a], Zhenkui Wang[b, c*],

[a] Nobel Denton marine services, Energy Systems, DNV, London, UK

[b] State Key Laboratory of Hydraulic Engineering Simulation and Safety, School of Civil Engineering, Tianjin University, Tianjin, China

[c] Department of Civil, Environmental and Geomatic Engineering, University College London, London, UK

Corresponding author: Zhenkui Wang, zhenkui@tju.edu.cn

ABSTRACT:

Previous experimental and numerical studies indicate that the stress state of sand at a specific depth changes significantly during the installation of a displacement pile. At a given depth level, the horizontal stress in sand increases as the end of pile approaches and reduces as the pile continues to penetrate and go past the sand element. This horizontal stress reversal, together with the large-strain deformation of the sand at the pile shaft, may cause a reduced accuracy in the calculation of pile capacity. In this paper, the micro-mechanical behaviour of sand developed around pile shaft during the installation of a closed-ended pile was studied using the two-dimensional Discrete Element Method (DEM). Sand assembly was modelled as uncrushable discs, and the closed-ended pile was modelled as a rigid clump which was made of a large number of overlapped discs with a fixed distance. The sand responses in terms of stress, strain and volume changes during the monotonic jacking of the closed-ended pile were investigated. Simulation results revealed micro-mechanical behaviours of the sand in both the interface zone "B" adjacent to the pile shaft and the far field zone "A" away from the pile. It was shown that the sand along the pile shaft at a small normalised distance to pile tip was subjected to a volume reduction as the pile goes past. As the pile drives deeper, the sand at a larger normalised distance to pile tip exhibited dilation. This captured process will give insights to the degradation of shaft friction at a given sand horizon.

KEYWORDS: friction degradation, displacement pile, discrete element method, sands

Notation

D_{pile}	pile diameter (mm)
E_p	particle Young's modulus (Pa)
F	applied force (N)
K_o	coefficient of earth pressure at rest
L	pile length (mm)
R_{pile} *or* R	pile radius = $D_{pile}/2$ (mm)
Z	soil depth (m)
Z_i	depth of monitored soil element (m)
d_{50}	particle diameter at 50% passing by area (mm)
d_{pp}	distance between centres of pile particles forming the pile-clump (mm)
g	gravity (m/s^2)
k_n	particle normal contact stiffness (N/m)
k_s	particle shear contact stiffness (N/m)
m_r	radius of measurement circle (mm)
r	radius of pile particles to create the pile-clump (mm)
u_x	lateral deflection (mm)
u_y	pile tip displacement (mm)
x	lateral distance from the centre of pile (m)
z	pile penetration depth (m)
z'	distance from monitored soil element to pile tip (m)
γ	bulk unit weight (kN/m^3)
μ	friction coefficient of the particles

1 INTRODUCTION

Pile foundations have been constructed widely for projects such as high-rise structures (Baziar, Rafiee, Lee, & Saeedi Azizkandi, 2018; Hokmabadi, Fatahi, & Samali, 2014; Kumar & Choudhury, 2018) or offshore wind turbines (Carswell et al., 2015; Duan, Cheng, & Xu, 2017). The mechanism underneath these structures is that the downward forces from the structures are supported by the upward forces mobilised by the soil-pile interfacial frictions and the pile tip resistances. The equilibrium between upward and downward forces is the critical criteria to foundation design (Åstedt, Weiner, & Holm, 1992; Axelsson,

2002; Bowman & Soga, 2005; Bullock, Schmertmann, Mcvay, & Townsend, 2005; Chow, Jardine, Brucy, & Nauroy, 1996; Fellenius, Riker, O'Brien, & Tracy, 1989).

The pile installation process will severely distort soil surrounding pile when the pile is pushed into soil (Duan, Cheng, & Liu, 2018; Liu, Yang, & Wang, 2014; Phuong, Tol, Elkadi, & Rohe, 2016; Valikhah, Eslami, & Veiskarami, 2019). Consequently, the properties of soil are changed after the installation; this is considered as the greatest uncertainty in foundation design (Galvis-Castro, Tovar-Valencia, Salgado, & Prezzi, 2019; Gupta, Salgado, Mitchell, & Jamiolkowski, 1998; Robinsky & Morrison, 1964; Yang, Tham, Lee, Chan, & Yu, 2006). There are two methods of pile installation: driven pile and jacked pile. Driven pile involves the use of hammers to provide impacts that are necessary to push a pile into the ground. The noise and ground vibration created by percussion piling are always a nuisance to residents in the vicinity of a foundation construction site, and may lead to damage to nearby structures and facilities. As an alternative to this environmentally unfriendly technique, a method of pile installation that involves the use of hydraulic jacks to press piles into the ground has gained increasing attention. This new technique is jacked pile which is free from noise and vibration (Yang et al., 2006). Hence, this study will mimic the jacked piles installation, as there is no unloading, however, the pile was loaded incrementally to ensure a quasi-static condition instead of pushing in with a constant speed. Pile shaft friction at a given sand horizon has been observed to decrease significantly during pile driving for decades (Hanna & Tan, 1973; Lehane, Jardine, Bond, & Frank, 1993; Vesic, 1970), this characteristic behaviour has been referred to as friction fatigue (Heerema, 1980). Numerous researches in both model scale and field test had identified that the change of sand volume in the interface shear zone during shearing played a critical role in friction fatigue of sand. The conventional methods to investigate the effect of pile installation on the surrounding soil include empirical methods, laboratory and field tests (Adejumo & Boiko, 2013; Fonseca, 2011; Phuong et al., 2016; M. F. Randolph, 2003), or numerical modelling (finite element method (FEM) and DEM). The empirical methods work reasonably well, but a good understanding of the micro mechanism of soil during the pile installation is lacking. The results from the experiments are good to understand the overall behaviour of soil under the pile installation effect, but the cost and time are relatively high. Moreover, there is still a lack of study in micro-mechanical level to quantify and reveal the evolution of stress, strain and volume of the surrounding sand during pile penetration to validate the proposed mechanisms. This is due to the limited data that can be secured from model scale experimental studies and large scale field tests alike. Numerical modelling has been used by some researchers (Lee & Salgado, 1999; Nicola & Randolph, 1993; Sagaseta & Whittle, 2001) to get a better understanding of the mechanism of friction fatigue. Compared with the experimental technique, the numerical modelling technique has been accepted as a more efficient approach to study the pile installation effect on soil. In general, FEM is better to model the continuous body, while DEM is better

to model the particle related problems. The simulation results based on FEM have been studied extensively (Broms, 1964; Dijkstra, Broere, Bezuijen, & Tol, 2008; Fischer, Sheng, & Abbo, 2007; Griffiths, 1982; Sloan & Randolph, 2010; Vermeer & Wehnert, 2004). But the continua assumption of soil when using FEM indicted that the technique did not consider the properties change of soil induced by pile installation. The mechanism for DEM is to use the deformable contacts and the time domain solution of the original equations based on the particles (Cheng et al., 2003). However, many of the previous studies (A. B. Huang, Ma, & Lee, 1993; M. J. Jiang, Harris, & Zhu, 2007; M. J. Jiang, Yu, & Harris, 2006; Macaro, Utili, & Martin, 2020) were based on small size models. Hence, the comparisons between the simulation results and experimental results remained qualitative rather than quantitative (Butlanska, Arroyo, Gens, & Catherine, 2014). The three-dimensional (3D) simulations of monotonic jacking have also been reported (Arroyo, Butlanska, Gens, Calvetti, & Jamiolkowski, 2011; Butlanska et al., 2014). However, the sizes of these simulations were even smaller to balance computation time. The studies by Loboguerrero (2005), M. Jiang, Dai, Cui, Shen, and Wang (2014) and Wang and Zhao (2014) have used DEM-2D to study the pile penetration, and the results have shown that DEM is able to capture the micro-mechanism during pile installation.

The main objective of this paper is thus to construct a DEM-2D model for simulating monotonic driven pile with a particular emphasis on adopting a high gravity field, and then to examine the penetration mechanisms from both macro-mechanical and micro-mechanical perspectives. The simulation approach was first verified by comparing the pile lateral resistance in the DEM simulation to that of a centrifuge test (Duan et al., 2017). Then, soil responses, including movement of particles, contact force mobilization and stress distribution, will be used to explain the friction degradation observed during pile penetration.

2 DEM MODEL

The PFC-2D program (Itasca, 2002) has been used in this DEM simulation. The contact model of linear springs has been used in this research. Figure 1 shows the schematic diagram of the DEM model for this study and Table 1 lists the input parameters used in the simulation. The units were listed assuming per unit length in the third dimension. Previous biaxial tests of circular particles assembly showed a typical critical state angle of friction of around 24^o (Z. Y. Huang, Yang, & Wang, 2008; Mingjing et al., 2010). The input particle stiffness ratio of 0.25 was found to affect the coefficient of earth pressure of the soil, giving a K_0 of 0.65, the detail will be shown in Figure 4. The same model were previously calibrated against the published 100g centrifuge data of a laterally loaded pile during monotonic (Duan & Cheng, 2016) and cyclic loadings (Duan et al. (2017). The selected monotonic data comparison will be shown in Figure 5. The model particle size distribution (PSD), given in Figure 2, was also the same as the previous publications. Sand particles

were simulated as discs ranging from 4.50 to 7.05mm in diameter with d_{50} of 5.85mm (see Figure 2). The subset of Figure 2 shows visually the shape and fabric of the particles in this PFC-2D model. The model pile was a close-ended pile of diameter D_{pile} = 45mm. It was generated by a DEM "clump" which was formed of a large amount overlapped pile-particles of r = 1.125mm. The distance between two adjacent particle centres was d_{pp} = 0.225mm, as is shown in the subset of Figure 1. With this excessive amount of overlap, although the density of individual pile particle was relatively small, the total weight of the created pile was similar to that of a steel pile. The input friction coefficient of the soil particles and the pile-particles was the same, representing a rough pile. The final penetration depth (pile length, L) was 514.8mm. The normalised pile diameter (D_{pile}/d_{50}) and the normalised pile length (L/d_{50}) were 7.7 and 88.0, respectively. Similar ratios were used in other DEM simulations, such as Loboguerrero (2005); Zhang and Wang (2015). The width and depth of this model were 2.4m and 1.05m respectively, which was twice bigger than that in Duan et al. (2018), hence the boundary effect could be minimised further. The total number of particles was 80,640. PFC-2D "measurement circles" with radius, m_r, of 50mm (i.e. approximately 8.5 times of d_{50}) were used to measure porosity and stresses of sand elements at one side of the symmetrical model. There are 9 VLs (vertical location) (VL1-VL9) in Figure 1 indicating 9 positions of measurement circle with the same x coordinate respectively. VL1 is 50mm away from the pile shaft. Meanwhile, the distance between the adjacent VLs is same as the radius of $m_{r,}$

Table 1. Input parameters for DEM model, and soil state at equilibrium.

Density of sand particles (kg/m^3)	2650
Density of pile particles (kg/m^3)	500
Friction coefficient of the particles μ (-)	0.5
Friction coefficient of pile & walls μ (-)	0.5
Particles Young's Modulus, E_p (Pa)	4e7
Contact normal stiffness of pile & particles, k_n (N/m)	8e7
Particle stiffness ratio (k_s/k_n)	0.25
Contact normal stiffness of walls, k_n (N/m)	6e12
Final average porosity - final equilibrium	0.185
Final average bulk unit weight of sand γ (kN/m^3)	21

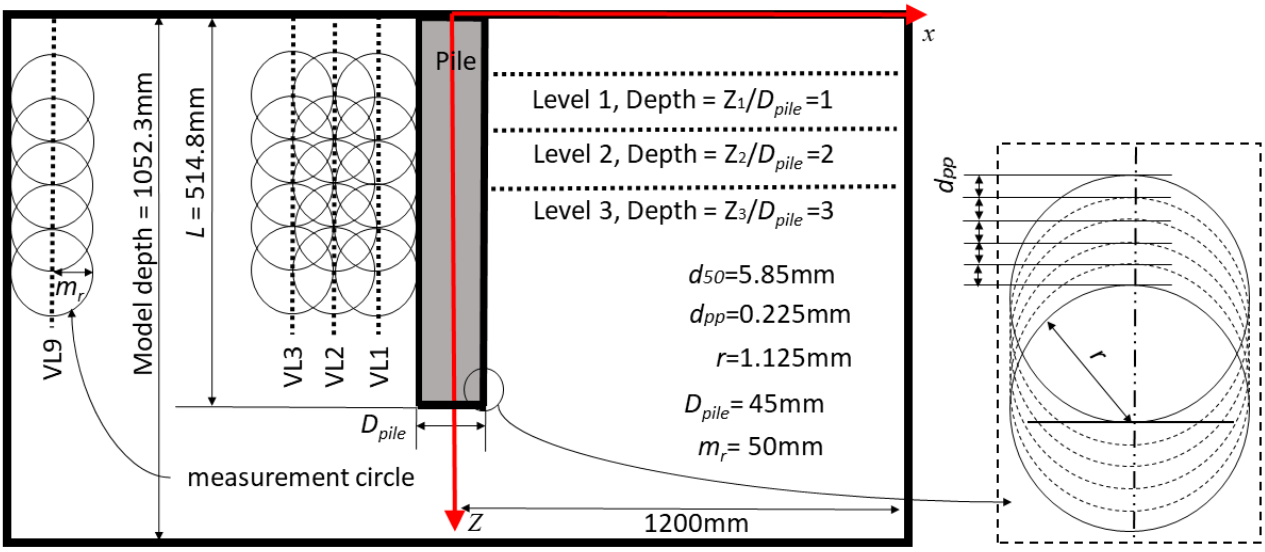

Figure 1. Schematic drawing of the model (VL1 to VL9 are nine columns of measurement circles, the components in this figure are not scaled)

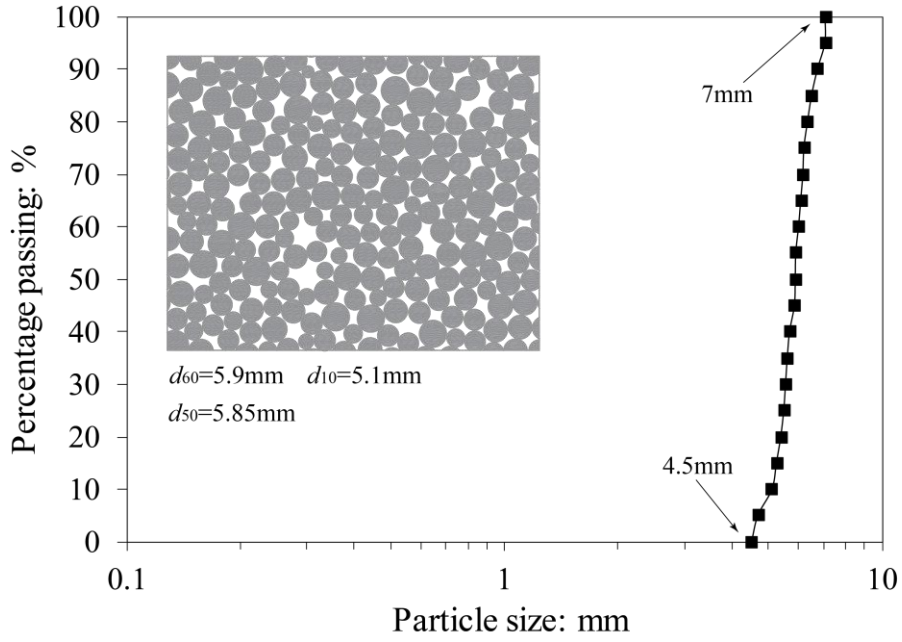

Figure 2. The particle size distribution of granular material

The DEM-2D analysis was performed using an increased gravity field of 100g. Following Duan & Cheng (2016), Duan et al. (2017) and Duan et al (2017), the Grid Method (GM) was used to create sand particles assembly with uniform porosity. At the beginning of sample preparation, the area of sand assembly was divided into layers, and each layer was subdivided into a number of square grids, each with a length of 100mm. During initial sample preparation, particles belonged to each grid were created with a target porosity of 0.25 and directly followed the PSD in Figure 2. This method of particle generation is called the

explosive method in the PFC manual. The particles were then assigned with properties listed in Table 1. In each grid, exactly 280 particles with the desired PSD were randomly generated and were enclosed by frictionless walls. All particles within each grid were initially cycled to reach equilibrium under a gravity of 1g. Within the same layer, after the first grid is in equilibrium, the next adjacent grid was created. When the whole sand layer was created and had reached their respective equilibrium, the temporary walls located in between every two grids were removed, and the whole layer of particles were cycled to equilibrium again under a gravity of 100g. Then, the positions of particles at the soil surface were temporarily fixed before the next layers of particles were created. The individual grid in the next layer where cycled to equilibrium at 1g, then the whole 2 layers were again cycled to equilibrium under 100g but now the fixed particles in between the layers are set free. This procedure was repeated until the whole soil sample was created to full height (Duan & Cheng, 2016). The target equilibrium level was achieved by setting the ratio of average unbalanced force to average contact force to be 10^{-5}. Figure 3**Error! Reference source not found.**(a) presents the distributions of porosity of the sand assembly at final equilibrium. It is shown that the 2D porosity decreases with depth and the average porosity is 0.185 which is equivalent to a void ratio of 0.23. Comparing the porosity measured from the five columns (VL1, VL2…VL5) of measurement circles at the same depth level, the porosity varies slightly, and the fluctuation range is 0.022 (±6%) which is acceptable. The main cause of this fluctuation is the disc sizes being relatively large compared to the real sand particles. Figure 3**Error! Reference source not found.**(b) shows the vertical and lateral stresses computed by DEM, and also the lateral stress distribution against the model and prototype depth (at 100g) when the coefficient of earth pressure K_0 is 0.65, calculated using the equilibrium bulk unit weight γ = 21 kN/m^3, as shown in Table 1.

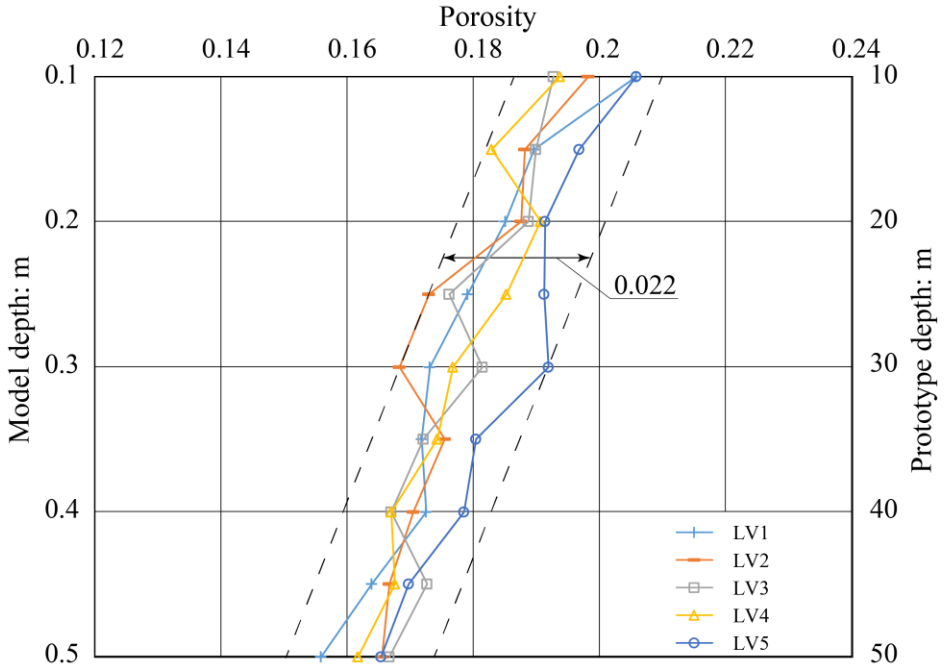

(a) The initial distribution of porosity

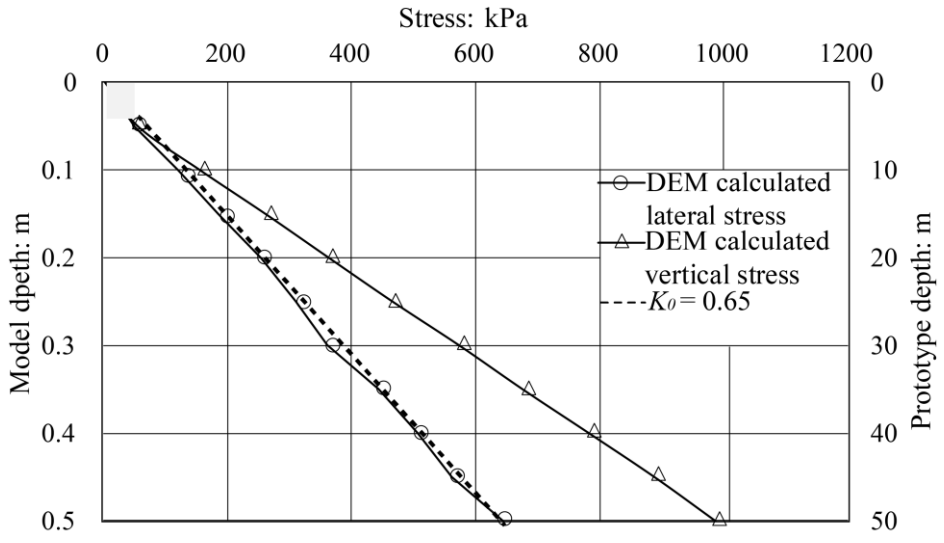

(b) Measured lateral and vertical stresses

Figure 3. Final equilibrium state before pile penetration (a) distributions of porosity, (b) vertical and lateral stresses

Using this GM, the particle assembly was created grid by grid, and each numerically cycled to reach a quasi-static equilibrium. The desired PSD was generated accurately and the number of particles in each grid was kept the same. As a result, not only could that the sand assembly in DEM model reach equilibrium within a shorter computational time, but also the stress field matched well with that observed in the

centrifuge testing at 100g. For instance, at the model sand depth of 0.5m (i.e. prototype depth of h=0.5×100=50m), the DEM computed vertical stress was slightly less than 1.0MPa, as shown in Figure 3(b). Due to the effect of particle size, this value is slightly different from the vertical prototype stress (γh=21x50=1.05MPa) under a gravity field of 100g. Also, this is because of the usage of the linear force-displacement law at particle contacts. Given that the contact stiffness ($k = F/u$) remains constant, the stress-strain relationship ($k = \sigma/\varepsilon$) remains unchanged. It should be noted that the unit of stresses is force per unit length here and the specific scaling laws, shown in Table 2, are similar to those of the centrifuge tests except for mass and force.

Table 2. Scaling Laws for DEM-2D with linear force-displacement law

Parameter	Acceleration	Displacement	Stress σ	Strain ε	Rotation	Mass	Force
Model/ Prototype	N_s	$1/N_s$	1	1	1	$1/N_s^2$	$1/N_s$

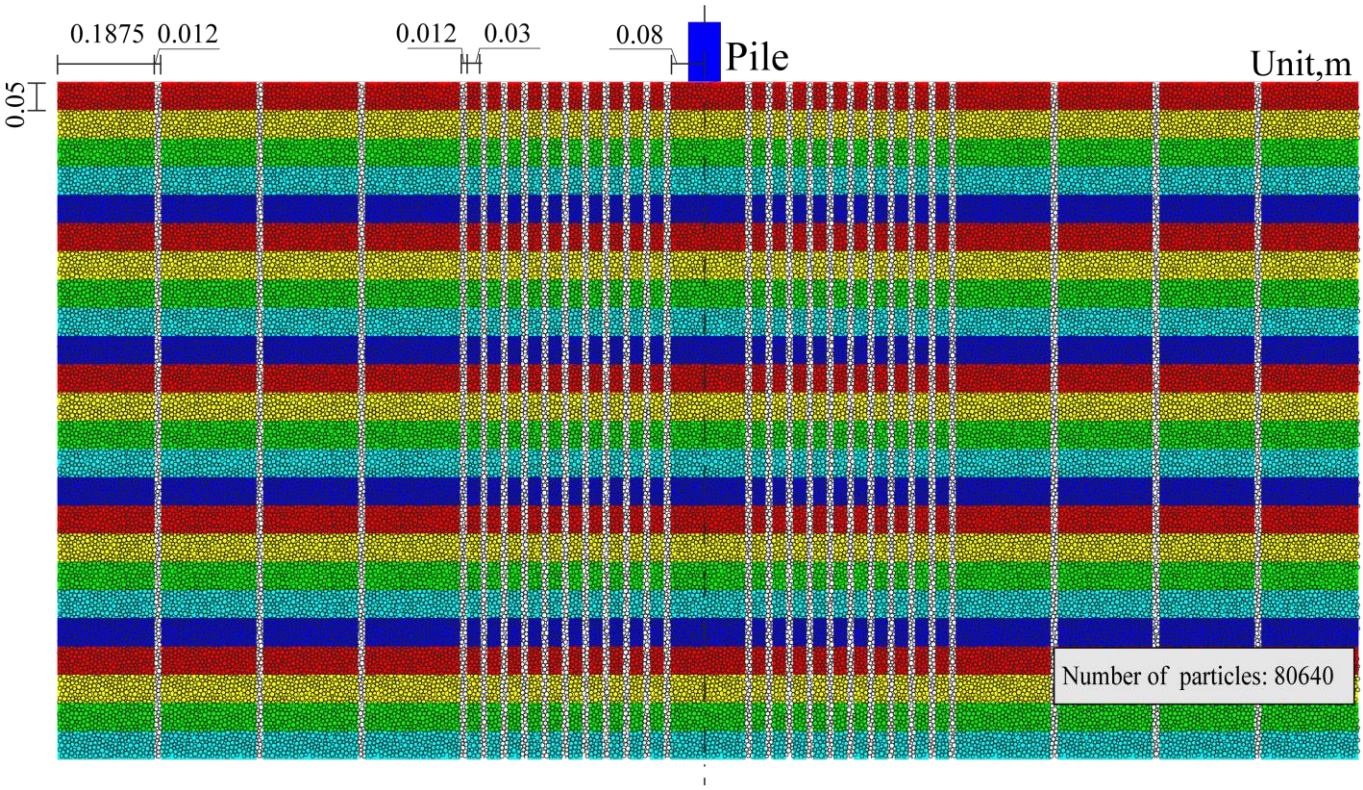

Figure 4. Coloured particles in DEM model

Error! Reference source not found.4 shows the coloured PFC model and the total number of particles is around 80,640. The thickness of each coloured layer is 50mm. Generally, there are two domains in this model. One region is near the pile, the other is far from the pile. For the district near pile, the distance

between two white vertical columns is 30mm. In the far area, the distance between two white vertical columns is 187.5mm. However, all the white colour columns have the same width which is 12mm. The layout of coloured model was designed to allow a better observation to the movement of particles during the pile installation.

It is worth illustrating in here that the results of the same numerical model but of a bored pile was previously reported by Duan and Cheng (2016), Duan et al (2017) and Duan et al (2018). The lateral load-deformation behaviour of the bored pile were previously calibrated with the centrifuge data of Klinkvort, Leth, and Hededal (2010). Figure 5 shows that although there is a clear difference in the lateral load-deflection curves for lateral eccentric loads applied at 2.5D_{pile} and 4.5D_{pile} or 6.5 D_{pile} above the pile head, the results matched reasonably well with the experimental centrifuge test data. Failure is defined as the load that corresponds to a settlement equal to 10% of the pile diameter. The figures show that, before failure, the results of DEM model are nearly same as the centrifuge experiment. Due to this good match at the relationship between lateral load and horizontal displacement, it is concluded that the numerical scheme adopted in the present investigation should be capable of modelling the pile-soil interaction under 100g gravity condition.

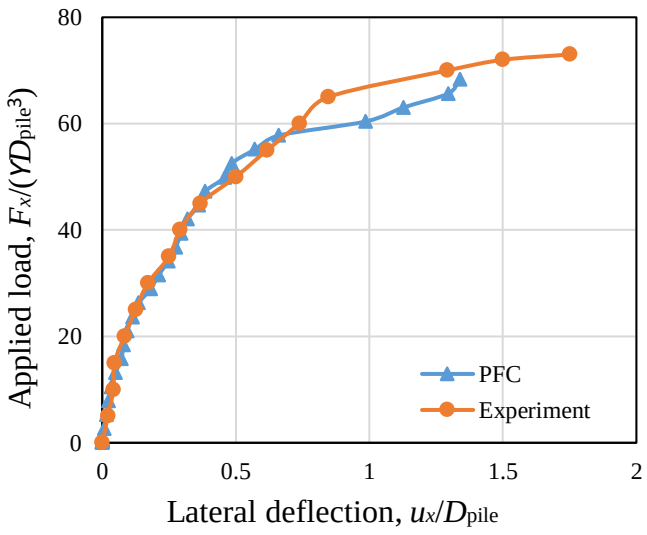

(a)

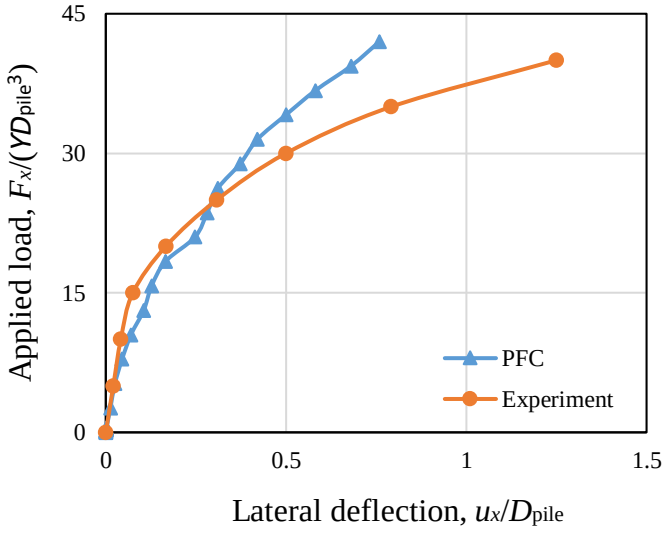

(b)

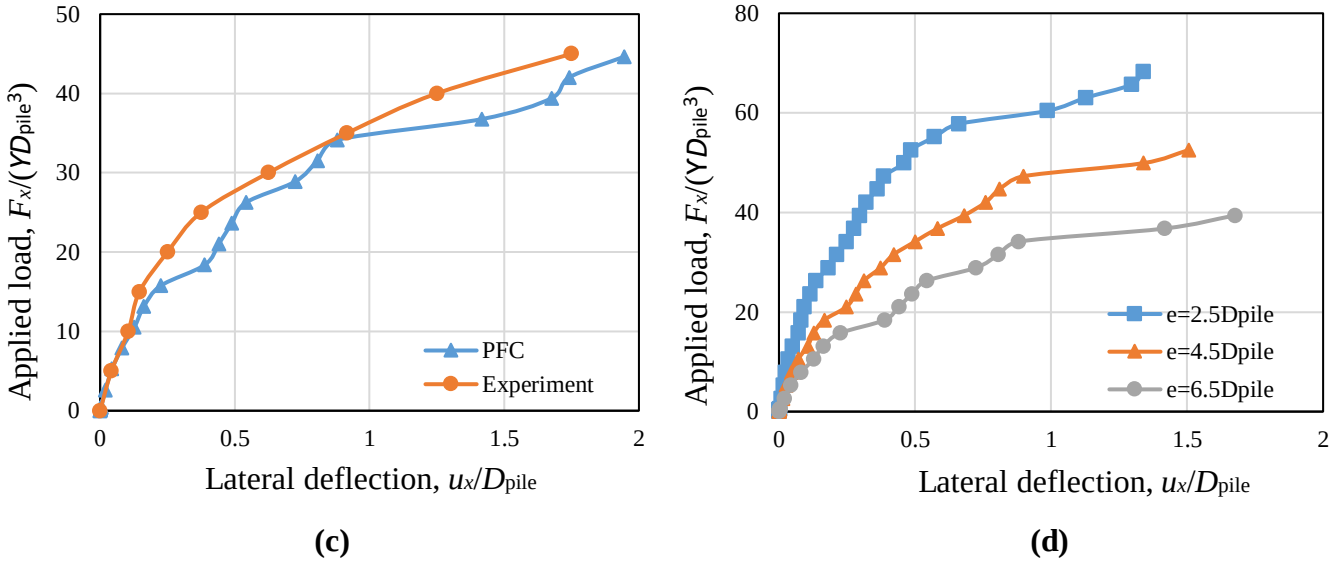

Figure 5. Comparison of DEM lateral response of pile with experimental test data of Klinkvort et al. (2010): (a) e=2.5D_{pile}; (b) e=4.5D_{pile}; (c) e=6.5D_{pile}; (d) comparison of three conditions.

3 FRICTION DEGRADATION

For the current pile installation investigation, the pile was pushed incrementally into the sand assembly by a stepwise increase of vertical load: 20kN, 40kN, 60kN, 80kN, 100kN, 120kN, 140kN and 160kN, applied at the top of the pile. At each applied load, the system was first numerically cycled until equilibrium, then the behaviour of the pile at the equilibrium load was recorded. Figure 6(a) shows the measured total, base and shaft forces on the pile under each increment of applied load, measured at each equilibrium pile tip depth, Z, for each vertical load. The total force is the sum of applied force and the weight of the pile. The shaft force is calculated by the vertical unbalance force of pile shaft. And the base force is the total vertical contact force at the bottom of the pile. Under the final applied vertical load of 160 kN, shaft resistance and end bearing resistance contribute to approximately 26% and 74% of the total pile resistance. Figure 6(b) represents the distributions of unit shaft resistance alongside the pile shaft under different applied loads. At this stage, in order to calculate the unit shaft resistance, the pile has been divided into many segments each with 18.9mm length. The sum of vertical unbalance force of each segment is then extracted for the representation of shaft resistance at this part. The length of 18.9mm is determined by the trial and error process. Integrating the unit shaft resistance for the entire length gives the total shaft resistance for each applied load shown in Figure 6(a). Figure 4(b) shows that, for many of the applied load cases, the unit pile shaft resistance increases with soil depth and reduces slightly near the tip of the pile. This pile shaft friction reduction behaviour was also observed by Vesic (1970) and M. Randolph, Dolwin, and Beck (1994). When

comparing the unit shaft resistance at a specific sand depth Z, the unit shaft resistance increases while the pile penetrates through the specific sand depth and then decreases when the pile penetrates further downward. A similar reduction of unit shaft resistance also has been observed in the field (Lehane et al., 1993). It is the purpose of the following sections to explain this observation.

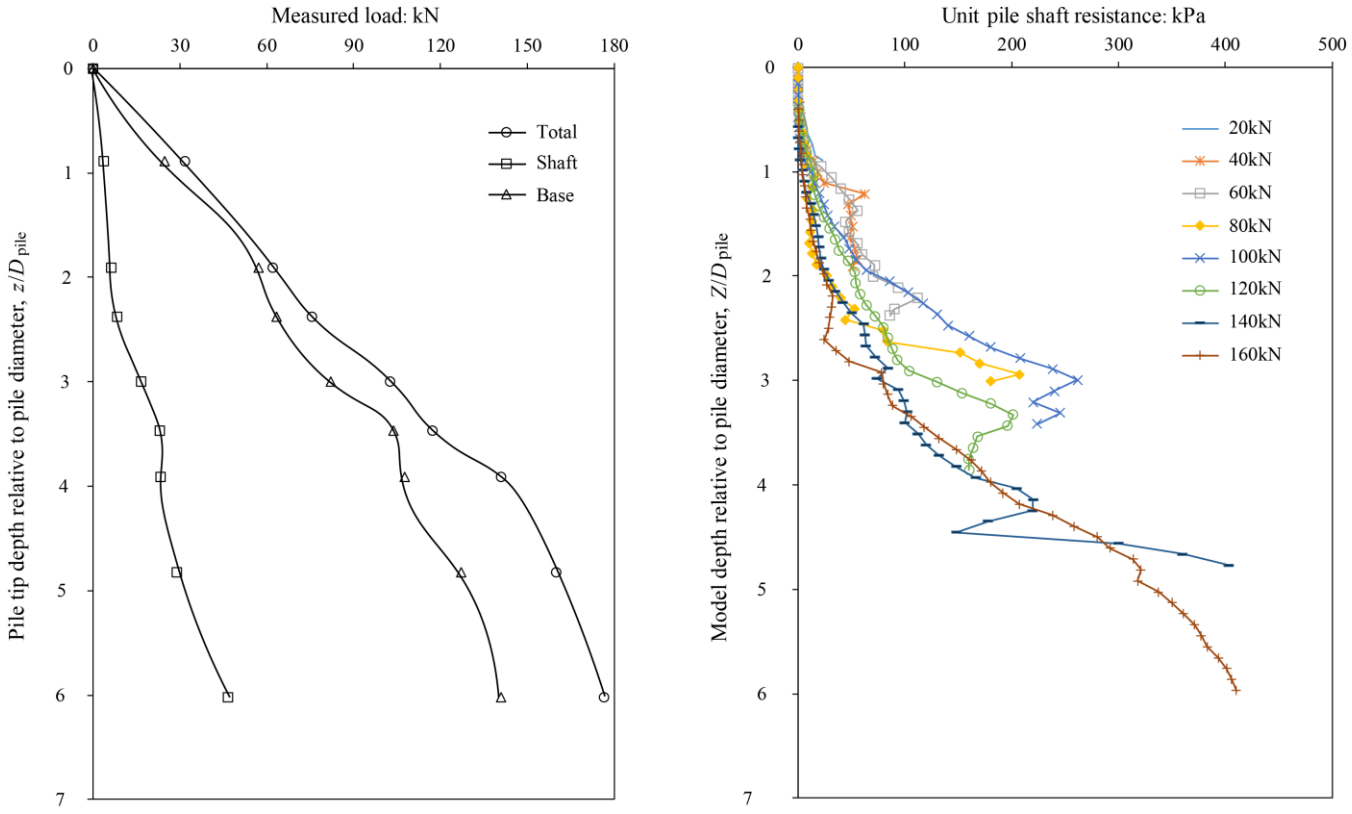

(a) (b)

Figure 6. (a) Pile penetration depth against measured total, shaft and based forces; (b) The unit shaft resistance along the pile right side shaft under applied loads.

By monitoring three soil elements (see Figure 1) at three different soil depths *Zi* (i = 1-3), Figure 7 plots the variations of the unit shaft resistance at the pile interface and the porosity of a sand assembly near the pile against the normalised distance from pile tip, $z'/D_{pile} = (z\text{-}Zi)/D_{pile}$,. Since *Zi* is a constant i.e. $1D_{pile}$, $2D_{pile}$ and $3D_{pile}$ (Figure 5(a), 5(b) and 5(c)) at its respective monitored soil depth, the normalised pile penetration z/D_{pile} is also shown as the top x-axes of in the figures. Note that the 37.8mm length division used here to calculate the unit shaft resistance is slightly longer than that of Figure 6. At shallower soil depths, $Z/D_{pile,}$ of 1 and 2 (Figure 7(a) and (b)), the maximum unit shaft resistance is always observed at a normalised distance, z'/D_{pile}, of 1.5, and it is coincident with the occurrence of a minimum porosity at the level. As the pile continues to penetrate, the unit shaft resistance decreases and approaches its respective constant values. Although the observed depth of Figure 7(b) is deeper than that of Figure 7(a), the sand assembly is still not

in a very dense state. The sand is compressed until it reaches a denser state, then soil volume starts to increase. As Figure 7(c) indicates the depth of observation is relatively deep (porosity ≈ 0.138 is reaching its minimum for these circular particles without crushing), therefore no further sand compaction is observed. Soil volume only increases as the pile drives past the point. At each level, the sand expands and dilates to a different constant values depending on soil depth.

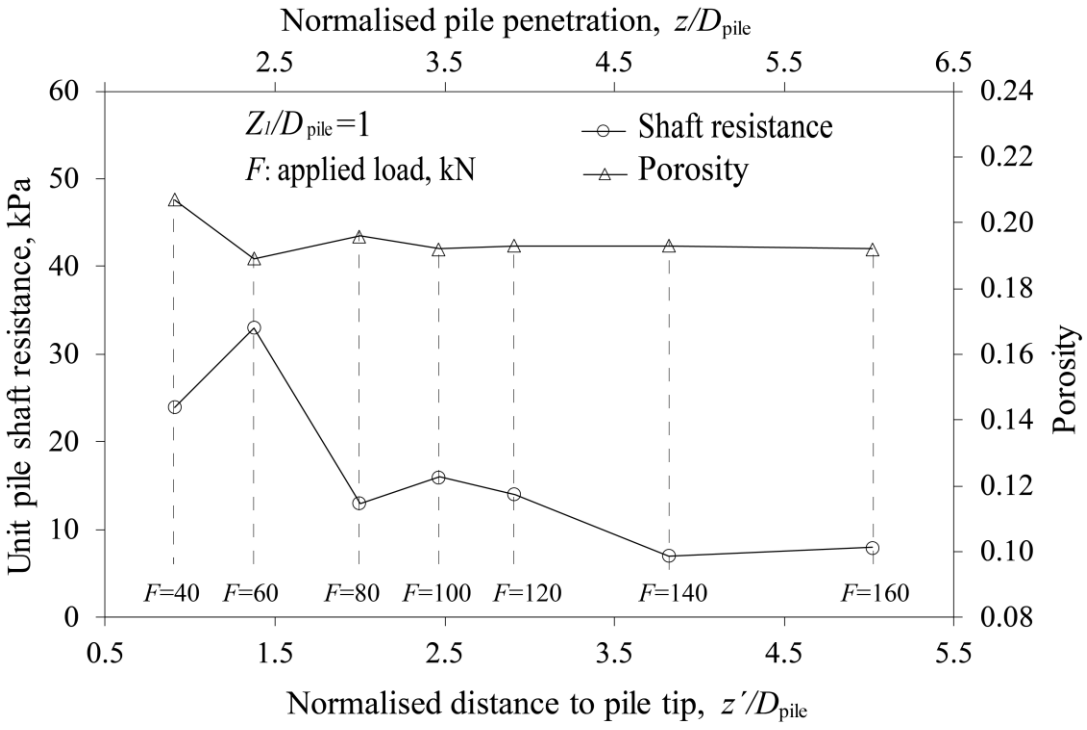

(a)

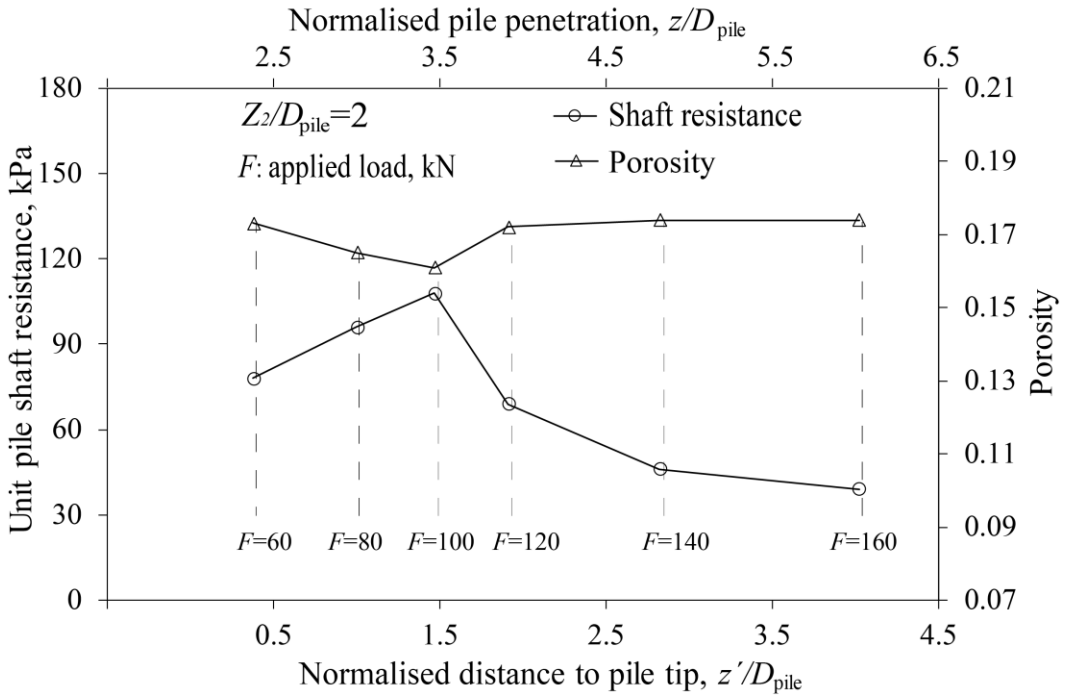

(b)

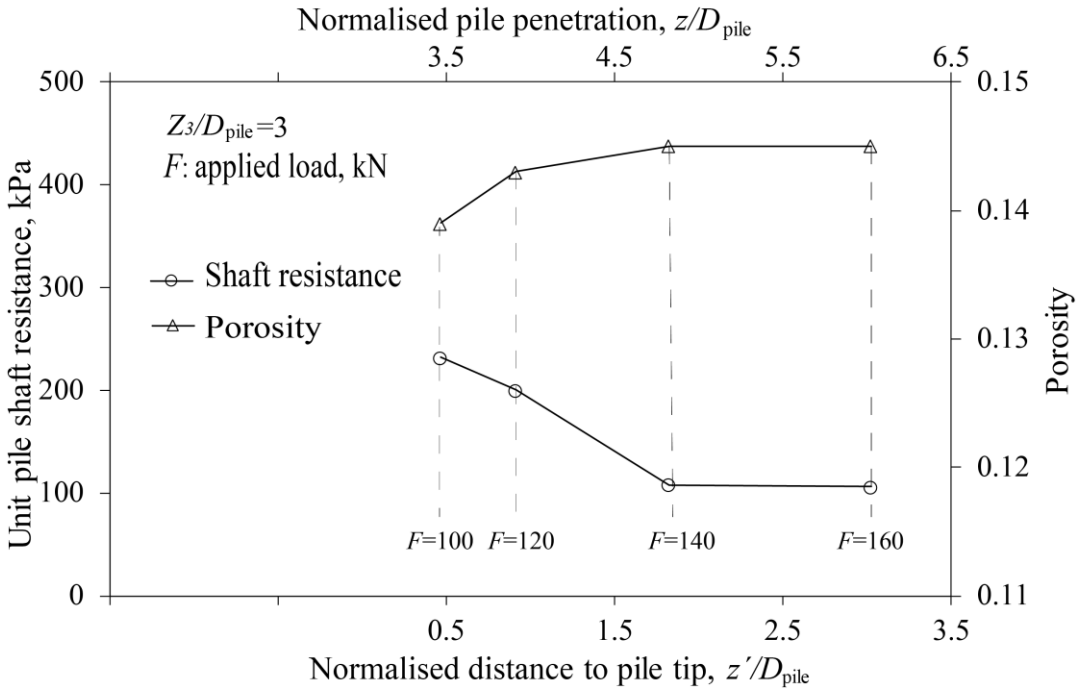

(c)

Figure 7. Unit pile shaft resistance and porosity change at three sand depths during pile installation (a) Z/D_{pile} = 1, (b) Z/D_{pile} = 2 (c) Z/D_{pile} = 3,

4 INTERFACE SHEAR ZONE

To investigate further about the phenomenon of this friction degradation, information at the interface shear zone is gathered, firstly by analysing the particle displacement field around the pile tip. The enlarged particles used in this model to simulate a model test have led to a quite small ratio of pile diameter to average grain diameter. However, the porosity or stress state in the observed shear zone should be the exact same as real sand. Due to the current efficiency of computer, we have tried to minimise the scale effect, such as by increasing the model dimension, and by decreasing the particle size. Based on the result of Figure 6, this numerical model at least can capture the basic characteristic of the phenomenon. The displacement vectors radiate from the pile tip in all directions similar to a cavity expansion, although the contours curve back to the pile shaft at shallow depth, similar to that was shown by White and Bolton (2004). The assembly's surface settlement profile can be more easily observed using the trajectory of particles movements (see subset of Figure 8(a)).

Figure 8(a) shows the accumulated displacement field of particles when the applied loading is 140kN. At this stage, all of the three soil elements at different depths have expanded and dilated, and shaft friction has reduced to a minimum according to Figure 5. According to the distribution of accumulated displacement, the most significant movements of particles have been found below the pile tip. This displacement field consists of intensely affected particles, which has been enlarged to reveal the deformation pattern. The particles along the upper part of pile shaft move diagonally downward to the pile. This is because of the gap

between pile shaft and soil has been formed when the pile is driving into the soil. At the same time, the sands in the area along the lower part of pile shaft move purely downward as the pile penetration. The reason for this phenomenon is due to the shearing action between pile shaft and sands. Figure 8(b) illustrates the contours of the accumulated displacement field of particles during pile penetration under the applied load of 140kN. As can been seen, the most significant movements of particles are below the pile tip. Particles along the upper part of pile shaft move diagonally downward; this is induced by the shaft downward movement. Particles along the lower part of pile shaft move purely downward due to the compression at pile end and the interface shearing at pile shaft. The total particle displacement at the pile tip is more than 200mm, of which only 5mm is in the horizontal direction. Figure 8(c) has captured the deformation of particles around the pile under the applied loading of 140kN. The original distance from pile shaft to the first white particle column is 80mm (≈16.5d_{50}). The width of each white particle column is 12mm (≈2d_{50}) and the distance between the columns is 30mm (≈5d_{50}). The thickness of each coloured particle layer is 50mm (≈8.5d_{50}). The figure indicates that the subsidence profile of particles is obvious and it extends to 5D_{pile}. The top layer particles (red colour) moves excessively downwards along the pile shaft. The relocation of this top particle layer to deeper zones during pile penetration is due to the created volume loss at the sand surface, resulting in a settlement profile at the sand surface.

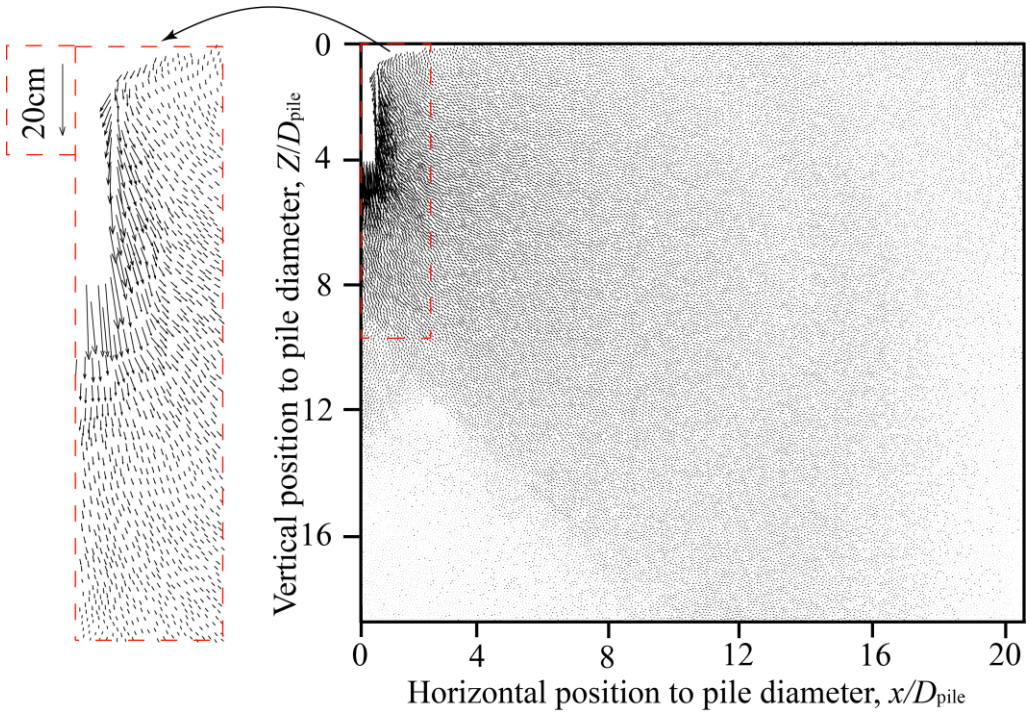

(a)

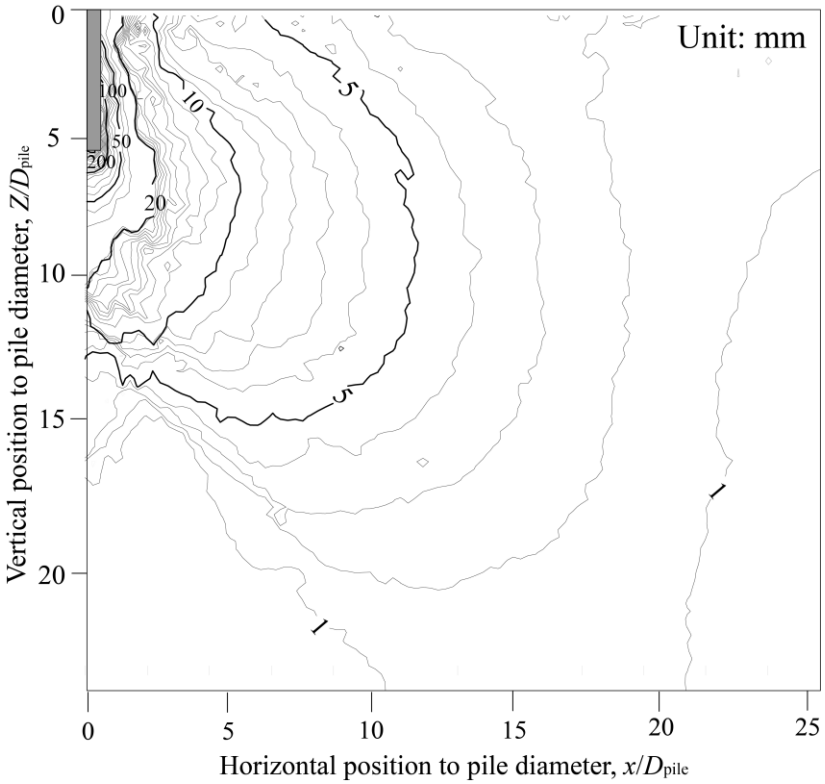
Unit: mm
100
50
200
20
10
5
3
1
1
Vertical position to pile diameter, Z/D_{pile}
Horizontal position to pile diameter, x/D_{pile}
0
5
10
15
20
25

(b)

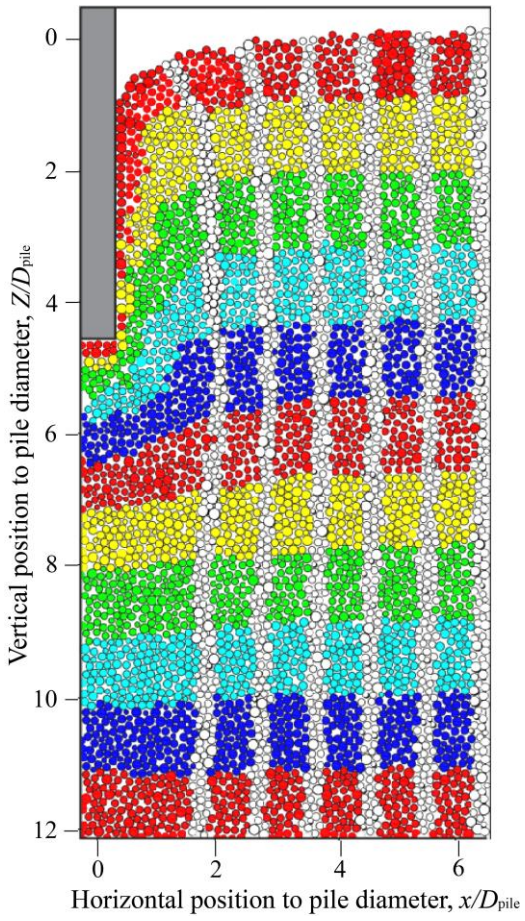
Vertical position to pile diameter, Z/D_{pile}
Horizontal position to pile diameter, x/D_{pile}
0
2
4
6
8
10
12

(c)

Figure 8. Particles displacement is shown using (a) accumulated displacement field around pile tip in DE2 case (F=140 kN) (b) contours of the accumulated particle displacement field magnitude: mm (F=140kN) (c) displacement of coloured particles in the DEM model under an applied load of 140kN

Several intervals of the particle movements during pile penetration were captured and analysed. Figure 9 shows the incremental vertical displacement contours under each 20kN incremental applied load: (a) 80kN-100kN, (b) 120kN-140kN and (c) 140kN-160kN. The contour patterns for increment 100kN-120kN are similar to those of 120kN-140kN so one was omitted. Many experimentalists adopted this method of using vertical displacement to obtain shear band thickness. In this study, it was found that the shear band thickness was approximately 4~6d_{50}. The contour at which there was a sudden change in density was chosen. It was found that the shear band thickness decreased from 4.8d_{50} to 4.3d_{50}, as found in Figure 7. For the loading increments of 80kN-100kN or 120kN-140kN, the critical states have not been reached. The shear band was initially thicker at a lower loading interval of 80kN-100kN, it then became thinner at the next two intervals (i.e. 100kN-120kN and 120kN-140kN). In the final interval, 140kN-160kN, the interface sands at all monitoring levels from Z/D_{pile} = 1 to Z/D_{pile} = 3 have reached the constant volume and constant shear stress critical state satisfactorily.

Another way of identifying the shear band is by particle rotation. **Error! Reference source not found.** shows the incremental rotation contours (in radian) of particles under the same loading increments. There is a similar reduction in the shear band thickness between 80kN-100kN and 120kN-140kN. The distinct rotation zone for the final load interval (i.e. 140-160kN) is shown in **Error! Reference source not found.**(c); the thickness is around 4.27d_{50}, showing also a similar small increase from the previous increment 120-140kN. The main difference between Figure 9 and **Error! Reference source not found.** is below the pile tip, where particles have experienced the most significant vertical displacement but without significant rotation.

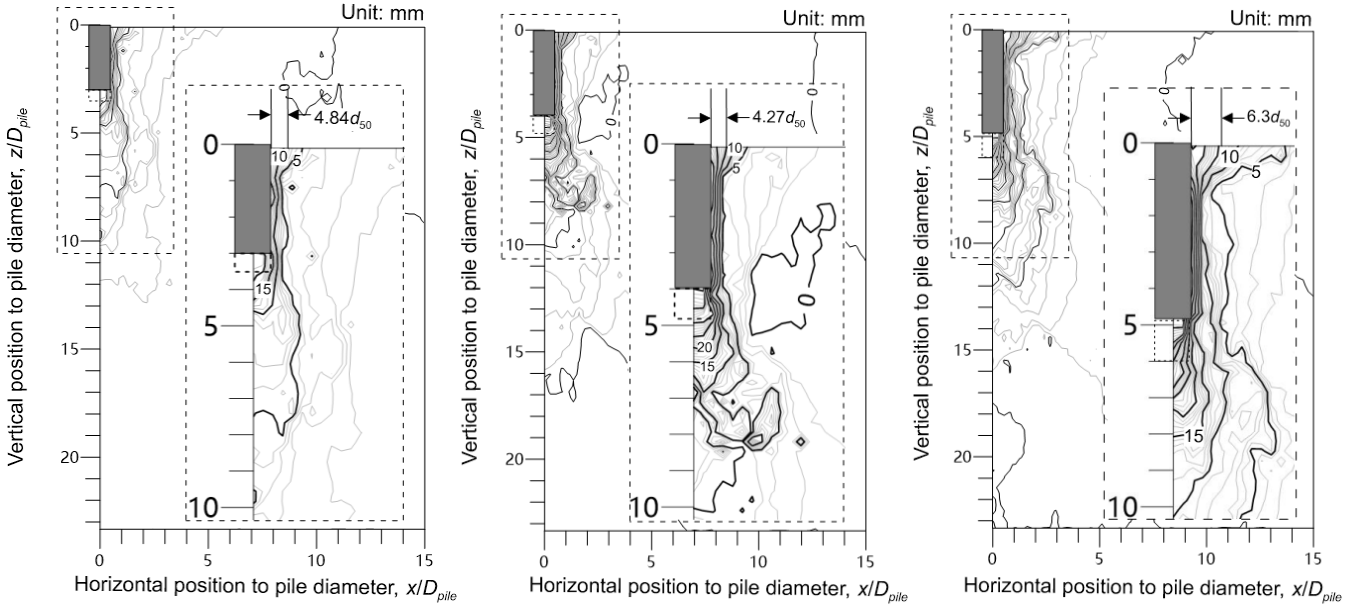

(a) 80kN-100kN (b) 120kN-140kN (c) 140kN-160kN

Figure 9. The contours of the incremental vertical displacement under axial force increments

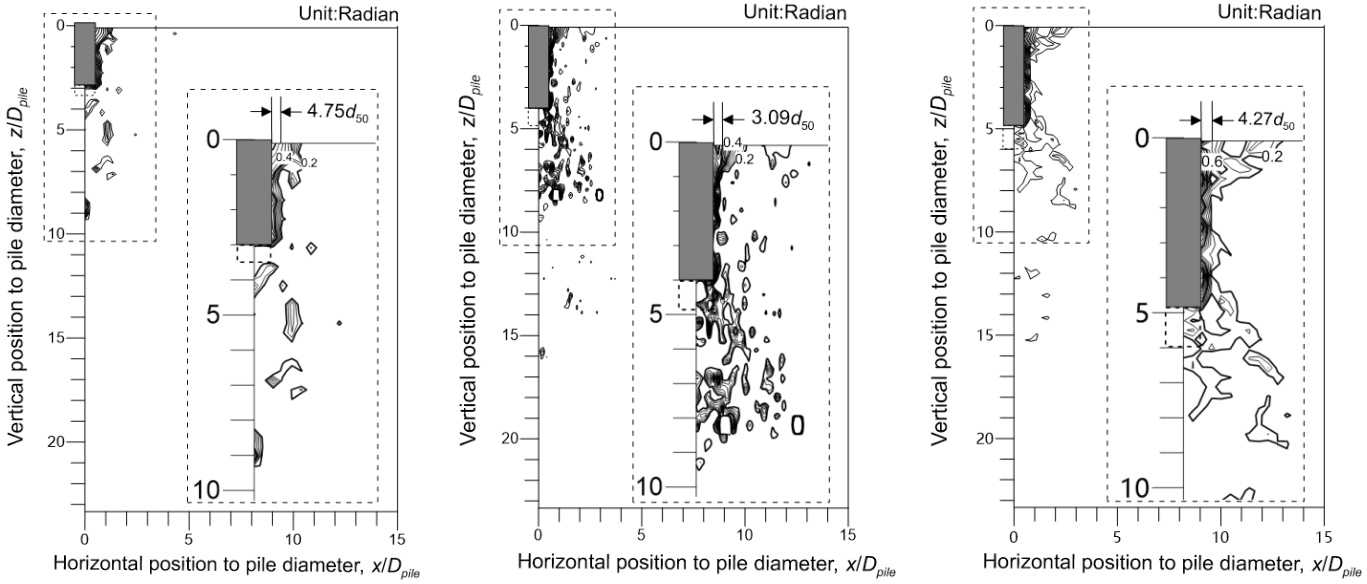

(a) 80kN-100kN (b) 120kN-140kN (c) 140kN-160kN

Figure 10. The contours of the incremental particle rotation contours under axial load increment

To accomplish the observation of the deformation of sand particles near the pile more clearly, Figure 11 expresses the movement and deformation of a chosen square-shaped sand element, whose area is 50mm^2, next to the pile shaft, at the initial normalised depth, Z/D_{pile}, of 2.38 under the applied load of 60kN. The initial location of this sand element is expected to be similar to that of $Z/D_{pile} = 2$, as shown in Figure 7(b). The sand element is compressed initially and the friction from the sand element to the pile shaft increases until the applied load of around 100kN. It can be seen from Figure 11 that most of the particles inside the element remain in the square-shaped area when being compressed at this stage, but the whole element

moves downloads as pile penetrates. When the applied load is larger than 120kN, the sand element starts to deform significantly with its own contained particles but particles that are in contact with the pile shaft move significantly downwards. When the four particles at the original vertexes of the element have been traced at each stage of the loading, it reveals the extensive shear deformation of the element and a significant amount of download movements of the particles interfaced with the pile. This is the stage when the shear band is seen with a reduction in thickness in Figure 9(b) and **Error! Reference source not found.**(b), and there is an overall increase in porosity outside the interface shear zone in Figure 7(b). This increase in porosity (apparent dilation) outside the shear zone gradually reaches its final state when unit shaft friction reduces to a minimum value at the larger pile load of 160kN. However, these final shaft frictions at critical state are related to the lateral stresses which will be further investigated in the next section.

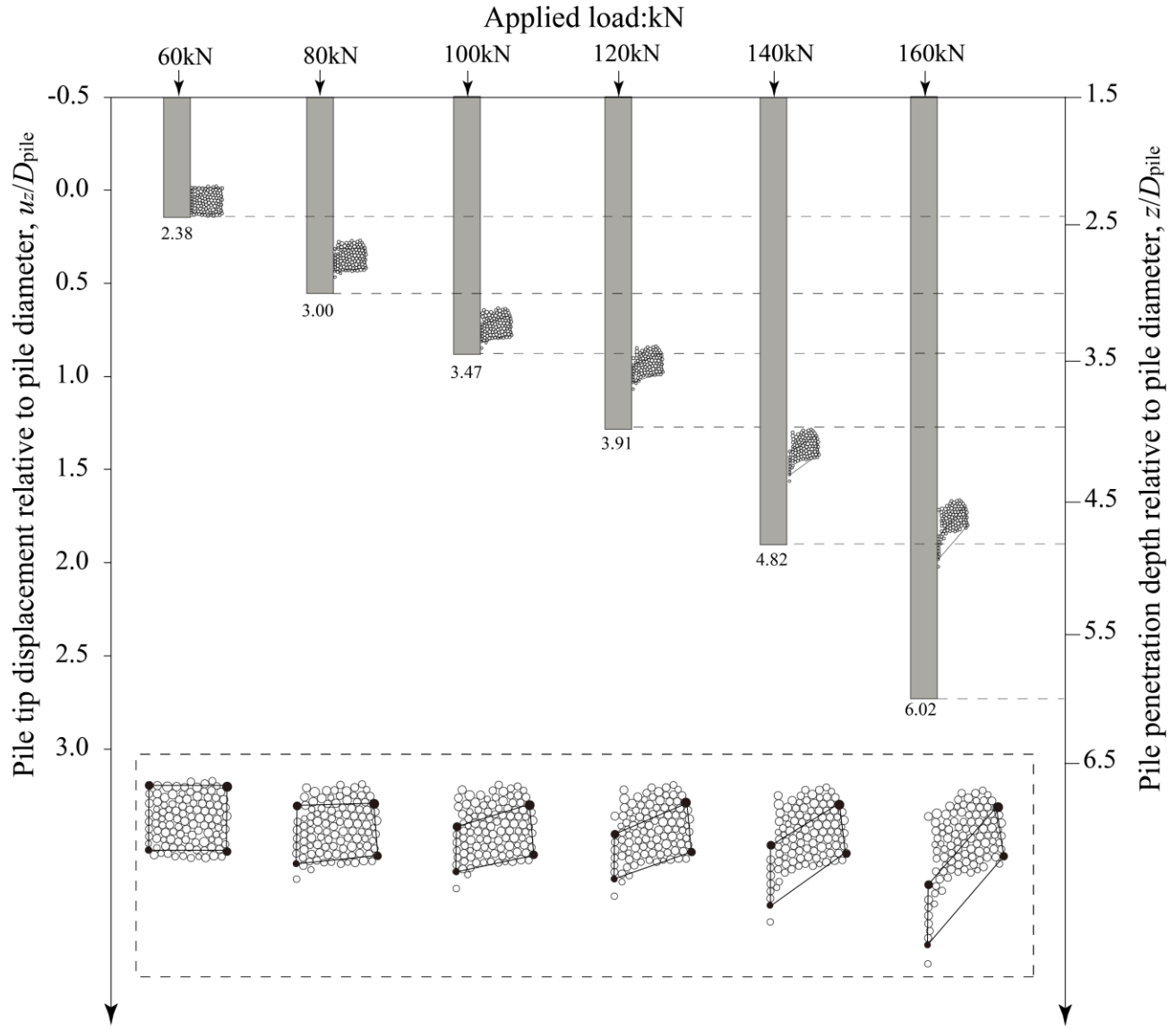

Figure 11. The deformation of a chosen sand element next to the pile shaft during pile installation

5 RELATING INTERFACE SHEAR ZONE AND FAR FIELD

White and Bolton (2004) proposed a mechanism that links the kinematic observation of a contractile interface zone to the degradation of shaft friction close to the pile tip. They studied the contraction of pile at interface zone B and related it to the reduction of the shaft friction. The evidence obtained from the current DEM simulations have revealed the same phenomenon. Zone A is away from the pile and it can be seen as a stiff spring that is fixed in the far field and exerts horizontal stress on the pile shaft. Their inter-relationship is explored in Figure 12 and Figure 13. The width of the interface zone B and the magnitudes of horizontal movements of sand particles in the far field zone A at two distinct depths (i.e. Z/D_{pile}=2 and Z/D_{pile}=3) are plotted in Figure 12; the corresponding changes in horizontal stress and porosity in the far field zone A are shown in Figure 13.

The DEM data shows explicitly that, for the pile penetration under the load increment of 80-100kN, at which the total pile tip penetration (i.e. z/D_{pile} is approximately 3) is small, the interface zone B (at the relatively shallow depth, Z/D_{pile} = 2) is relatively thick, as shown in Figure 12(a) and Figure 10(a). And the sand in far field zone A is being compressed (i.e. sand particles moves away from the pile) giving a negative change in porosity, as shown in Figure 13. The lateral stress increases in the far field zone A. This increase in the lateral spring stress has led to an increase in shaft resistance in the interface zone B. On the other hand, for the pile penetration under the load increment of 120-140kN, at which the pile tip penetration is relatively deeper (z/D_{pile} is approximately 4), the interface zone B at the pile shaft location (at soil depth Z/D_{pile} = 3) becomes thinner as shown in Figure 12(b). The sand particles representing the stiff spring in the far field zone A are being unloaded during shearing giving positive change in porosity (i.e. dilation) as shown in Figure 13. The horizontal stress decreases in far field zone A has led to a decrease in shaft resistance in zone B.

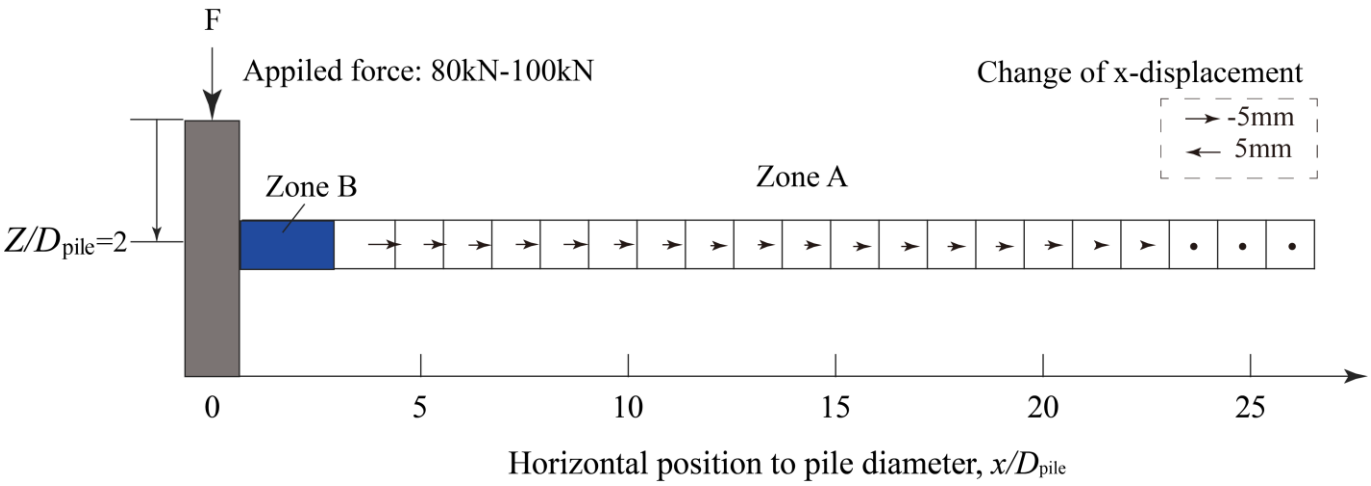

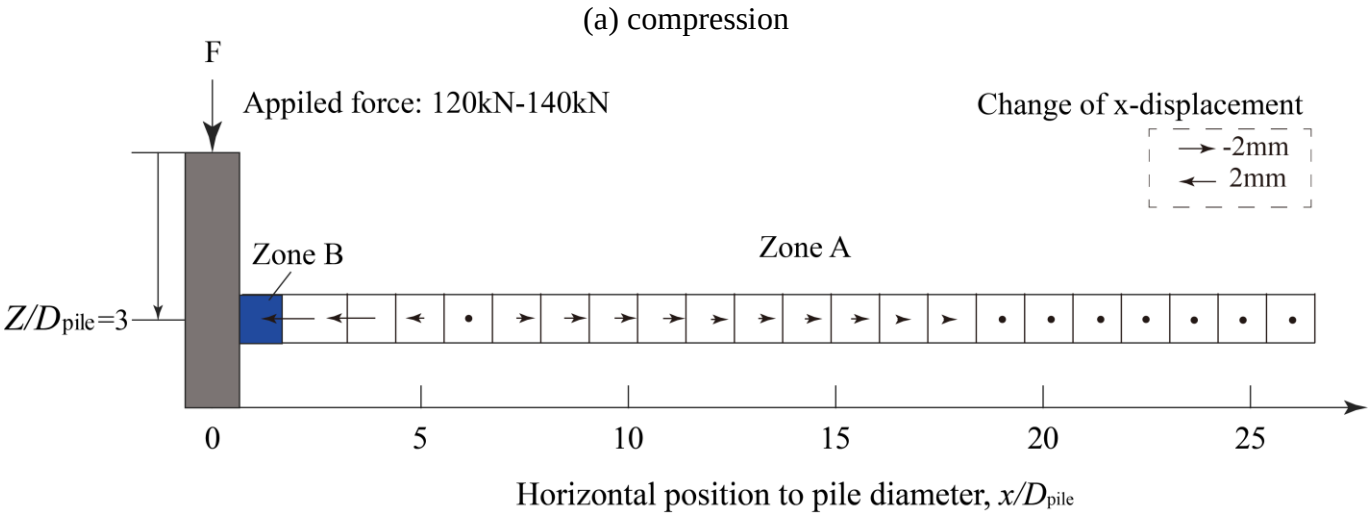

Figure 12. The change of x-displacement of zone A

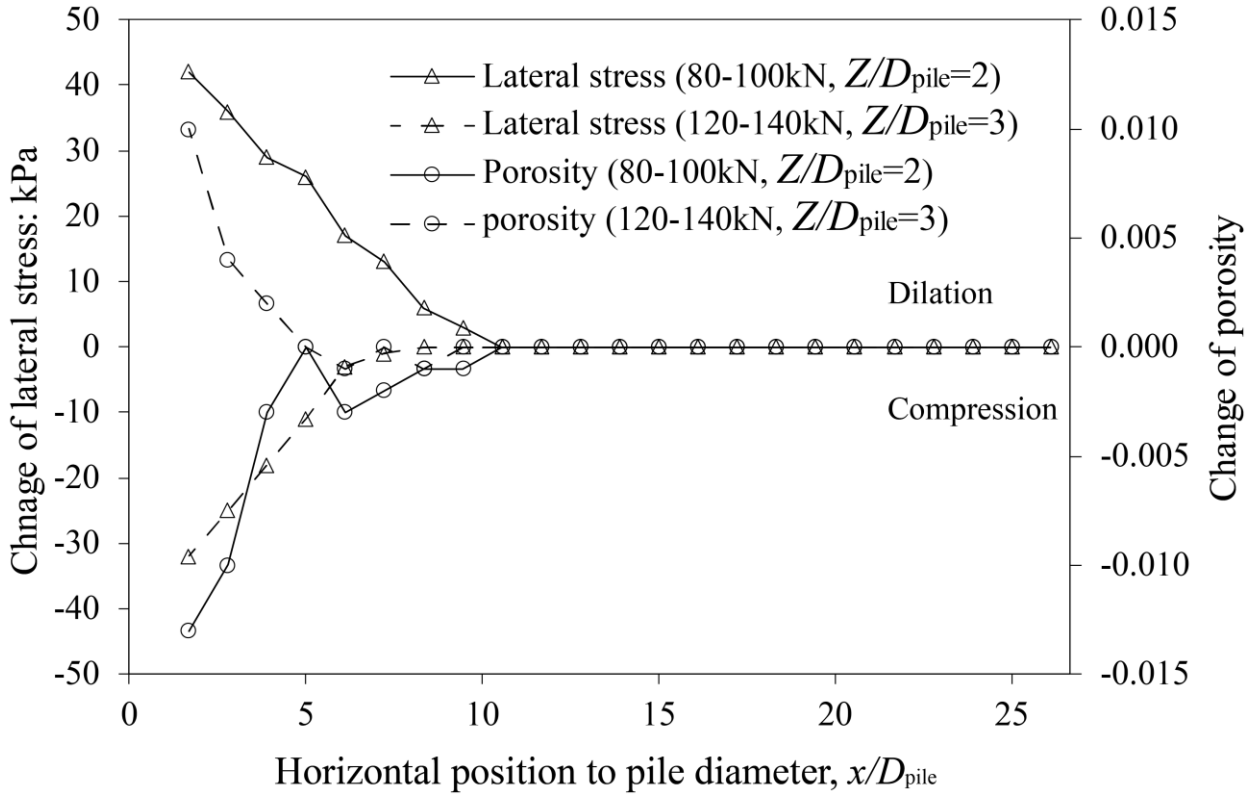

Figure 13. The change of lateral stress and porosity of zone A

6 DISCUSSION

Based on the data presented, it appears that there are two regimes of sand response during pile penetration. Consider a soil element at a soil depth Z/D_{pile} = 2 when the applied load increment is 80kN-100kN, the negative change in porosity happens together with a positive change in lateral stress (Figure 11). At this zone, sand is being compressed (Figure 5) as lateral stress increases, as the pile initially drives past.

Particles in zone B are being compressed, together with particles in zone A move away from the pile as the stiff spring is compressed. The influence zone is large with a x-displacement neutral point as far as x/D_{pile} = 24 (see Figure 10(a) and Figure 6b), although the lateral stress neutralises at around x/D_{pile} = 10 (Figure 11). This phenomenon is similar to a cavity expansion. It happens nearer to the pile tip as the pile just goes past the soil element up to around z'/D_{pile}=1.5 and at shallow depth (Figure 5). But shearing also distorts the soil element (Figure 9). This shear-induced unit shaft resistance increases as the stiff spring is being loaded and lateral stress increases. Later on, as the pile penetrates deeper into ground and the normalised distance from the pile tip is higher at z'/D_{pile} >1.5 (see Figure 5), for example, when the applied load increment is 120-140kN, the positive change of porosity implies the volume of the soil element increases (Figure 11). This happens as lateral stress decreases (stiff spring is unloaded). The particles in zone B moves toward the pile (Figure 10(b)). This is because of the large strain deformation of the soil as is seen in Figure 6, creating a gap at the pile-soil interface. The soil actually moves into this gap. The shear-induced unit shaft resistance at this stage reduces as the stiff spring in the far field is being unloaded hence lateral stress decreases.

A careful look into Figure 10(b) finds two neutral x-displacement points at around x/D_{pile} = 6 and x/D_{pile} = 19. The figure shows that particles in zone B moves towards the pile into the gap, whereas particles further away from pile are still moving away from the pile, that generates two neutral points. This interesting phenomenon in particular around x/D_{pile} = 6 away from the pile also influences stress zone. A careful look at Figure 11 shows that the lateral stress in this case neutralises at around x/D_{pile} = 6 instead of x/D_{pile} = 10. Please note that this stress relaxation could be even more obvious as particle crushing happens at the proximity of the pile. When this happens, the volume dilation of soil may not occur but further volume reduction occurs due to particle crushing.

7 CONCLUSIONS

The displacement pile installation was simulated using a two-dimensional DEM numerical model with the PFC-2D program. The initial ground condition before pile penetration was carefully created using the Grid Method and the stress field for the sand assembly in the initial condition matched well with the stress field developed from the prototype scale. The sand particles movements around the pile have been investigated in detail through the high precision of data extraction and analysing technique in the simulation. Friction degradation at the pile shaft was observed during the pile penetration.

- The interface shear zone along the pile shaft was captured in the simulation. It is shown that the thickness varied between 4-6d_{50} depending on the method of measurement. Because the interface zone B is thin, only the porosity and stresses data in the far field zone A were measured in the

simulation. In the far field zone A, it was shown that the changes of porosity and stresses reduce with increasing of the distance from the pile and diminish at around x/D_{pile} = 10 in the simulations.

- Shaft resistance along the pile was dependent on both the sand depth, Z/D_{pile}, and the distance from pile tip, z/D_{pile}. At shallow sand depth with Z/D_{pile} smaller than 2, the sand away from the shear band was loose enough and was capable of having an initial compression when shaft friction increased to its peak at around 1.5 z'/D_{pile}. This sand compression in the far field zone A was found to be related to the relatively thick interface shear zone B. This meant that when the interface shear zone B increased in thickness, the sand in the far field at zone A was being compressed hence there was an increase in the lateral stress in far field zone A. On the other hand, sand dilation in far field zone A began at the same time with shaft friction degradation. When this happened, the interface shear zone B reduced in thickness which then reduced the lateral stress and increased the porosity at zone A.
- At the deeper locations (i.e. Z/D_{pile} = 3), the idealised sand was very dense, so no initial sand compression was observed. As the pile penetrated and passed the observed depth, the shaft resistance immediately started to reduce and the sand in the far field zone A started to dilate until a constant value. Both porosity and shaft friction for the sand at a normalised depth, z'/D_{pile}, of 3 were found to reached their respective constant values, at around 5.5 z/D_{pile}.

Acknowledgements

Funding: This study was funded by: Zhejiang Provincial Natural Science Foundation (grant No. LQ18E090009); Open Fund Project of MOE Engineering Research Center of Geotechnical Drilling and Protection, China University of Geosciences (Wuhan); Open Fund Project of MOE Key Laboratory of Soft Soil and Geoenvironmental Engineering, Zhejiang University (grant number 2018P07); National Natural Science Foundation of China (grant No. 52078465)

Reference

Adejumo, T. W., & Boiko, I. L. (2013). Effect of Installation Techniques on the Allowable Bearing Capacity of Modeled Circular Piles in Layered Soil. *International Journal of Advanced Technology & Engineering Research, 2*(8), 1536-1542.

Arroyo, M., Butlanska, J., Gens, A., Calvetti, F., & Jamiolkowski, M. (2011). Cone penetration tests in a virtual calibration chamber. *Géotechnique, 61*(6), 525-531.

Åstedt, B., Weiner, L., & Holm, G. (1992). *Increase in bearing capacity with time for friction piles in silt and sand.* Paper presented at the Proceeding Nordic Geotechnical Meeting, Aalborg, Denmark.

Axelsson, G. (2002). *A Conceptual Model of Pile Set-Up for Driven Piles in Non-Cohesive Soil.* Paper presented at the International Deep Foundations Congress.

Baziar, M. H., Rafiee, F., Lee, C. J., & Saeedi Azizkandi, A. (2018). Effect of Superstructure on the Dynamic Response of Nonconnected Piled Raft Foundation Using Centrifuge Modeling. *International Journal of Geomechanics, 18*(10).

Bowman, E. T., & Soga, K. (2005). Mechanisms of setup of displacement piles in sand: laboratory creep te. *Revue Canadienne De Géotechnique, 42*(5), 1391-1407.

Broms, B. B. (1964). Lateral Resistance of Piles in Cohesive Soils. *J.s.m.f.d, 90*(3), 123-156.

Bullock, P. J., Schmertmann, J. H., Mcvay, M. C., & Townsend, F. C. (2005). Side Shear Setup. I: Test Piles Driven in Florida. *Journal of Geotechnical & Geoenvironmental Engineering, 131*(3), 292-300.

Butlanska, J., Arroyo, M., Gens, A., & Catherine, O. S. (2014). Multi-scale analysis of cone penetration test (CPT) in a virtual calibration chamber. *Canadian geotechnical journal, 51*(1), 51-66.

Carswell, W., Johansson, J., Løvholt, F., Arwade, S. R., Madshus, C., Degroot, D. J., & Myers, A. T. (2015). Foundation damping and the dynamics of offshore wind turbine monopiles. *Renewable Energy, 80*, 724-736.

Cheng, Y. P., Nakata, Y., Bolton, M.D. (2003). Discrete element simulation of crushable soil. *Géotechnique, 53*(7), 633-642.

Chow, F. C., Jardine, R. J., Brucy, F., & Nauroy, J. F. (1996). Effects of Time on Capacity of Pipe Piles in Dense Marine Sand. *Journal of Geotechnical & Geoenvironmental Engineering, 124*(3), 254-264.

Dijkstra, J., Broere, W., Bezuijen, A., & Tol, A. F. V. (2008). 44 DENSITY CHANGES NEAR AN ADVANCING DISPLACEMENT PILE IN SAND. *Dutcgeo.ct.tudelft.nl*.

Duan, N., Cheng, Y., & Liu, J. (2018). DEM analysis of pile installation effect: comparing a bored and a driven pile. *Granular Matter, 20*(3), 36.

Duan, N., Cheng, Y., & Xu, X. (2017). Distinct-element analysis of an offshore wind turbine monopile under cyclic lateral load. *Geotechnical Engineering, 170*(6).

Fellenius, B. H., Riker, R. E., O'Brien, A. J., & Tracy, G. R. (1989). Dynamic and Static Testing in Soil Exhibiting Set-Up. *Journal of Geotechnical Engineering, 115*(7), 984-1001.

Fischer, K. A., Sheng, D., & Abbo, A. J. (2007). Modeling of pile installation using contact mechanics and quadratic elements. *Computers & Geotechnics, 34*(6), 449-461.

Fonseca, A. V. D. (2011). Effects of the construction method on pile performance: evaluation by instrumentation - part 1: experimental site at the University of Campinas. *Soils & Rocks, 34*(1), 51-64.

Galvis-Castro, A. C., Tovar-Valencia, R. D., Salgado, R., & Prezzi, M. (2019). Compressive and Tensile Shaft Resistance of Nondisplacement Piles in Sand. *Journal of Geotechnical and Geoenvironmental Engineering, 145*(9), 04019041.04019041-04019041.04019020.

Griffiths, D. V. (1982). Computation of bearing capacity factors using finite elements. *Géotechnique, 32*(3), 195-202.

Gupta, R. C., Salgado, R., Mitchell, J. K., & Jamiolkowski, M. (1998). Calibration Chamber Size Effects on

Penetration Resistance in Sand. *Journal of Geotechnical & Geoenvironmental Engineering, 127*(127), 878-888.
Hanna, T. H., & Tan, R. H. S. (1973). The behavior of long piles under compressive loads in sand. *Canadian Geotechnical Journal, 10*(3), 311-340.
Heerema, E. P. (1980). *Predicting pile driveability: Heather as an illustration of the" friction fatigue" theory.* Paper presented at the Ground Engng.
Hokmabadi, A. S., Fatahi, B., & Samali, B. (2014). Assessment of soil–pile–structure interaction influencing seismic response of mid-rise buildings sitting on floating pile foundations. *Computers & Geotechnics, 55*(2), 172-186.
Huang, A. B., Ma, M. Y., & Lee, J. S. (1993). A micromechanical study of penetration tests in granular material. *Mechanics of Materials, 16*(1–2), 133-139.
Huang, Z. Y., Yang, Z. X., & Wang, Z. Y. (2008). Discrete element modeling of sand behavior in a biaxial shear test. *Journal of Zhejiang University SCIENCE A*.
Itasca. (2002). PFC2D-particle flow code. Version 3.0. In: Itasca Consulting Group Inc.
Jiang, M., Dai, Y., Cui, L., Shen, Z., & Wang, X. (2014). Investigating mechanism of inclined CPT in granular ground using DEM. *Granular Matter, 16*(5), 785-796.
Jiang, M. J., Harris, D., & Zhu, H. H. (2007). Future continuum models for granular materials in penetration analyses. *Granular Matter, 9*(1-2), 97-108.
Jiang, M. J., Yu, H. S., & Harris, D. (2006). Discrete element modelling of deep penetration in granular soils. *International Journal for Numerical & Analytical Methods in Geomechanics, 30*(4), 335-361.
Klinkvort, R. T., Leth, C. T., & Hededal, O. (2010). *Centrifuge modelling of a laterally cyclic loaded pile.* Paper presented at the Physical Modelling in Geotechnics.
Kumar, A., & Choudhury, D. (2018). Development of new prediction model for capacity of combined pile-raft foundations. *Computers & Geotechnics, 97*(5), 62-68.
Lee, J. H., & Salgado, R. (1999). Determination of pile base resistance in sands. *Journal of Geotechnical Geoenvironmental Engineering, 125*(8), 673-683.
Lehane, B., Jardine, R., Bond, A. J., & Frank, R. (1993). Mechanisms of shaft friction in sand from instrumented pile tests. *Journal of Geotechnical Engineering, 119*(1), 19-35.
Liu, M., Yang, M., & Wang, H. (2014). Bearing behavior of wide-shallow bucket foundation for offshore wind turbines in drained silty sand. *Ocean Engineering, 82*(82), 169-179.
Loboguerrero, S. (2005). DEM analysis of crushing around driven piles in granular materials. *Géotechnique, 55*(8), 617-623.
Macaro, G., Utili, S., & Martin, C. M. (2020). DEM simulations of transverse pipe–soil interaction on sand. *Géotechnique*, 1-16.
Mingjing, Jiang, Hehua, Zhu, Xiumei, & Li. (2010). Strain localization analyses of idealized sands in biaxial tests by distinct element method. *Frontiers of Architecture & Civil Engineering in China*.
Nicola, A. D., & Randolph, M. (1993). Tensile and Compressive Shaft Capacity of Piles in Sand. *J Geotech Eng, 119*(12), 1952-1973. doi:doi:10.1061/(ASCE)0733-9410(1993)119:12(1952)
Phuong, N. T. V., Tol, A. F. V., Elkadi, A. S. K., & Rohe, A. (2016). Numerical investigation of pile installation effects in sand using material point method. *Computers & Geotechnics, 73*, 58-71.
Randolph, M., Dolwin, R., & Beck, R. (1994). Design of driven piles in sand. *Géotechnique, 44*(3), 427-448.
Randolph, M. F. (2003). Science and empiricism in pile foundation design. *Géotechnique, 53*(10), págs. 847-876.
Robinsky, E. I., & Morrison, C. F. (1964). Sand Displacement and Compaction around Model Friction Piles. *Canadian geotechnical journal, 1*(2), 81-93. Retrieved from https://doi.org/10.1139/t64-002. doi:10.1139/t64-002
Sagaseta, C., & Whittle, A. J. (2001). Prediction of ground movements due to pile driving in clay. *Journal of Geotechnical Geoenvironmental Engineering, 127*(1), 55-66.
Sloan, S. W., & Randolph, M. F. (2010). Numerical prediction of collapse loads using finite element

methods. *International Journal for Numerical & Analytical Methods in Geomechanics*, *6*(1), 47-76.
Valikhah, F., Eslami, A., & Veiskarami, M. (2019). Load–displacement behavior of driven piles in sand using CPT-based stress and strain fields. *International Journal of Civil Engineering*, *17*(12), 1879-1893.
Vermeer, P., & Wehnert, M. (2004). *Numerical analyses of load tests on bored piles*.
Vesic, A. S. (1970). Tests on Instrumented Piles, Ogeechee River Site. *Journal of the Soil Mechanics and Foundations Division*, *96*(2), 561-584.
Wang, J., & Zhao, B. (2014). Discrete-continuum analysis of monotonic pile penetration in crushable sands. *Canadian geotechnical journal*, *51*(10), 1095-1110.
White, D. J., & Bolton, M. D. (2004). Displacement and strain paths during plane-strain model pile installation in sand. *Géotechnique*, *54*(6), 375-397.
Yang, J., Tham, L. G., Lee, P. K. K., Chan, S., & Yu, F. (2006). Behaviour of jacked and driven piles in sandy soil. *Géotechnique*, *56*(4), 245-259.
Zhang, Z., & Wang, Y. (2015). Three-dimensional DEM simulations of monotonic jacking in sand. *Granular Matter*, *17*(3), 359-376.